Biomaterials Advances 185 (2026) 214889

Contents lists available at ScienceDirect

Biomaterials Advances

journal homepage: www.journals.elsevier.com/materials-science-and-engineering-c

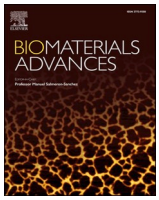

Engineered bioaerogel particles: a core–shell approach to adenosine delivery for wound healing

Beatriz G. Bernardes [a,b], Clara Sousa [a], Maria Rosaria Sellitto [c], Ana Iglesias-Mejuto [b,d], Pasquale Del Gaudio [c], Raquel Costa [a,e], Carlos A. García-González [b,*], Ana Leite Oliveira [a,*]

[a] Universidade Católica Portuguesa, CBQF - Centro de Biotecnologia e Química Fina – Laboratório Associado, Escola Superior de Biotecnologia, Rua Diogo Botelho 1327, 4169-005, Porto, Portugal
[b] AerogelsLab, Department of Pharmacology, Pharmacy and Pharmaceutical Technology, I+D Farma group (GI-1645), iMATUS and Health Research Institute of Santiago de Compostela (IDIS), Universidade de Santiago de Compostela, E-15782, Santiago de Compostela, Spain
[c] Department of Pharmacy, University of Salerno, 84084, Fisciano, Italy
[d] Research Institute for Medicines (iMed.ULisboa), Faculty of Pharmacy, Universidade de Lisboa, Av. Professor Gama Pinto, Lisboa, 1649-003, Portugal
[e] Biorbis, Unipessoal LDA, Edifício de Biotecnologia da Universidade Católica Portuguesa, Rua Diogo Botelho 1327, 4169-005, Porto, Portugal

ARTICLE INFO

Keywords:
Core–shell aerogels
Silk proteins
Chronic wound healing

ABSTRACT

Chronic wounds require advanced biomaterials that combine structural integrity with controlled drug delivery. This study reports the development of novel core–shell aerogel particle systems based on silk fibroin (SF), silk sericin (SS), and alginate (ALG) designed for the controlled delivery of adenosine (ADO), a molecule known for anti-inflammatory and angiogenic properties, which can play a role in the process of wound healing. Leveraging the biocompatibility, porosity, and tunable properties of these natural polymers, a core–shell architecture was engineered by combining prilling and supercritical CO_2 drying technologies. The particles were composed of a SF/ALG core and an ALG or an ALG combined with a SS shell. All particle compositions exhibited high porosity (94–97%) and a pH-responsive swelling behavior. FTIR and PCA confirmed structural integrity and composition. ADO encapsulation achieved moderate loading and controlled-release profiles, influenced by shell composition. Biological evaluation confirmed biocompatibility in human dermal fibroblasts, keratinocytes, and endothelial cells. Although no significant differences were observed, the reductions in pro-inflammatory cytokines and angiogenesis by ADO-loaded particles in CAM assays support their potential as multifunctional wound-healing platforms.

1. Introduction

Wound healing is a dynamic process involving hemostasis, inflammation, proliferation, and remodelling, all coordinated by cells and signalling molecules to restore skin function [1–3]. Disruptions, particularly during the inflammatory phase, can hinder healing and lead to chronic wounds characterised by persistent exudate and protease activity that impede tissue repair [2]. Contemporary wound dressings are essential for protecting injuries, maintaining a moist environment, and promoting healing. However, many traditional materials are limited in their ability to promote tissue regeneration or prevent infection effectively [2,4]. These materials promote healing by absorbing exudate, protecting the wound, improving oxygenation, and reducing the risk of infection [4]. They can also deliver proteins, drugs, or growth factors directly to the wound site [3–5]. Among them, bio-based aerogels—i.e., ultralight, highly porous materials derived from natural polymers—stand out for their biocompatibility, biodegradability, and exceptional fluid absorption, making them promising candidates for managing highly exudative wounds [2,6].

Silk proteins and alginate (ALG) are biopolymers with significant promise in wound healing and tissue regeneration [3,7]. Silk, mainly composed of fibroin (SF) and sericin (SS), offers biocompatibility, regenerative capacity, and anti-inflammatory properties, and can be easily functionalized [1,3]. ALG, a polysaccharide derived from brown seaweed, is valued for its non-toxicity, biocompatibility, strong absorption, and ability to maintain a moist environment [7–9]. Because of these benefits, both have been studied individually as carriers for drug delivery in wound treatments [3,7]. By combining different

* Corresponding authors.
E-mail addresses: carlos.garcia@usc.es (C.A. García-González), aloliveira@ucp.pt (A.L. Oliveira).

https://doi.org/10.1016/j.bioadv.2026.214889
Received 29 January 2026; Received in revised form 19 March 2026; Accepted 13 April 2026
Available online 15 April 2026

biopolymers, it is possible to create advanced materials with tailored properties, improving their effectiveness for biomedical applications.

Core–shell particles comprise a solid core and a distinct outer shell, combining the advantages of both materials in one single structure [10]. By choosing suitable materials and modifying their surfaces, these particles can be tailored for biomedical uses like imaging, biosensing, and wound healing improving treatment effectiveness, reducing side effects, and making them more suitable for deep wounds [2,3,11,12]. Core–shell systems have recently enabled advanced responsive microcapsules, including gelatin methacryloyl/ALG structures produced by microfluidics that incorporate curcumin nanoparticles in the shell with Vascular Endothelial Growth Factor (VEGF) in the core for Near-Infrared Radiation-activated antibacterial action, as well as ultrasound-responsive hydrogel microcapsules containing an oxygen-rich perfluorocarbon core and a curcumin-loaded shell that synergistically enhance oxygen release, sonodynamic activity, and anti-inflammatory effects to accelerate healing of infected chronic wounds [13,14]. They are particularly useful for encapsulating bioactive compounds, with fabrication methods such as prilling, coaxial electrospinning, and supercritical drying allowing precise control over their properties [15–17]. Several studies have demonstrated their potential in wound care. For instance, pectin–alginate microcapsules achieved high doxycycline loading and sustained release [16], while other systems used zein–cellulose or nanofibers for controlled delivery of curcumin, ibuprofen, or human epidermal growth factor (hEGF) [18,19]. Photothermal-responsive and antimicrobial core–shell systems have also shown promise in promoting angiogenesis and accelerating healing in infected wounds [20,21]. SF is widely used in core–shell systems for its biocompatibility and adaptable structure, supporting applications from drug delivery to tissue engineering. It has been used to develop magnetic nanoparticles for sustained curcumin release in cancer therapy [22], and coaxial nanofibers with curcumin-loaded SF cores and vancomycin-loaded chitosan/Polyvinyl Alcohol (PVA) shells for ocular treatments [23]. SF has also been integrated into polyaniline-based scaffolds to enhance fibroblast growth [24], and into electrospun nanofibers with poly(ε-caprolactone) shells for tissue regeneration [25]. Additionally, ciprofloxacin-loaded ALG–SF aerogel beads have demonstrated both antimicrobial and hemostatic properties [26]. A multilayer core–shell nanofibrous structure was developed using amine-modified SS, whose chemical functionalization enhances stability and bioactivity and enables coaxial electrospinning with PVA as the supportive core and Polylactic Acid (PLA)/poly(ε-caprolactone) (PCL) as the mechanical shell, with methylamine-modified SS showing the best thermal, mechanical, and biological performance [27]. However, there remains a notable gap in the creation of core–shell particles, especially aerogel-based systems, that combine both SF and SS, representing a promising yet underexplored area for biomedical innovation. Adenosine (ADO) is a promising molecule for wound healing due to its anti-inflammatory and regenerative properties. However, its hydrophilic nature leads to rapid release and significant drug loss in solid formulations, as observed in previous ADO-loaded SF aerogel microparticles [28]. To address this limitation, a core–shell architecture combining ALG with SF and SS, was proposed to enhance ADO retention, modulate release kinetics, and preserve bioactivity under physiological conditions. Two particle systems were developed: one with an ALG shell and SF/ALG core, and another incorporating SS into the shell, representing the first integration of SS in core–shell aerogels for wound healing. The resulting formulations exhibited high porosity, pH-responsive swelling, and non-cytotoxicity, while promoting anti-inflammatory and angiogenic effects. The core–shell design effectively protects ADO and improves the sustained release, positioning these particles as innovative multifunctional platforms for chronic wound treatment.

2. Materials and methods

2.1. Materials and reagents

SF was extracted from *Bombyx mori* cocoons supplied by the Portuguese Association of Parents and Friends of Mentally Disabled Citizens (APPA-CDM, Porto, Portugal). Lithium bromide (LiBr, ≥99%) and absolute ethanol (≥99.8%) were sourced from Honeywell (Wabash, IN, USA). Adenosine (ADO, ≥99%; CAS: 68–51-7), sodium carbonate (Na_2CO_3, ≥99.8%), and zinc chloride ($ZnCl_2$) were obtained from Sigma-Aldrich (St. Louis, MO, USA). Sodium alginate (ALG) was purchased from Carlo Erba (Milan, Italy), and high-purity carbon dioxide (99.99%) was provided by GASIN (Leça da Palmeira, Portugal). The human keratinocyte cell line (HaCat) was acquired from Cell Line Services (Oppenheim, Denmark), while human dermal fibroblasts (HDF, P10858) and human dermal microvascular endothelial cells (HDMEC, P10861) were obtained from Innoprot (Derio, Spain).

2.2. Core-shell particles production

Core–shell particles were formulated using ALG, SF, and SS. SF and SS were derived from *Bombyx mori* cocoons using previously established extraction protocols [29,30]. For SF, cocoons were degummed in a Na_2CO_3 solution, then dissolved in LiBr (9.3 M), followed by dialysis with a 2 kDa membrane to remove salts (Sigma-Aldrich, St. Louis, MO, USA). The resulting solution was concentrated by heating. SS was obtained by boiling chopped cocoons in deionized water (1:100 w/v) for 1 h, filtering out the fibers, and reducing the volume by evaporation.

The particle core was composed of ALG blended with SF with or without ADO, while the shell consisted of ALG alone or in combination with SS. To prepare the core phase, a 2% ALG stock was mixed with a ~ 7% SF solution to achieve final concentrations of 0.1% ALG and 5% SF (w/v). The shell phase followed a similar approach, substituting SS for SF where applicable.

Five varieties of core–shell particles (Table 1) were prepared using a prilling device (Encapsulator B-360, Büchi Labortechnik AG, St. Gallen, Switzerland) equipped with a coaxial nozzle and supported by a double piston pump (Fusion 4000, Chemyx Inc., supplied by KR Analytical, Sandbach, Cheshire, UK). The inner and outer nozzles had diameters of 450 μm and 600 μm, respectively, and the optimized flow rates applied were 7.5 mL/min for the core solution and 20 mL/min for the shell solution. The nozzle was maintained at 35 °C with a vibration frequency of 250 Hz.

The particles were collected in a gelling ethanolic bath to form gel core–shell beads via crosslinking with a 0.1 M $ZnCl_2$ solution. To improve particle stability and remove residual reactants, they were gently agitated in absolute ethanol for 5 min. A solvent exchange process was then conducted over 3 days, with fresh absolute ethanol added every 24 h.

Aerogels were produced by supercritical CO_2 drying of alcogel particles using a reactor system (Parr Instrument Company, Illinois, USA). The drying process involved a 2.5 h drying phase at 120 bar, followed by a 1 h static phase at 130 bar, and a 1 h drying phase at 125 bar. Depressurization was carefully controlled to maintain the structural integrity of the aerogel particles. ADO-loaded aerogel particles were stored at 4 °C with silica desiccant to maintain stability, while the remaining samples were kept at ambient temperature in a desiccator. A schematic of the core–shell particle production process is presented in Fig. 1.

2.3. Size, particle size distribution, morphology, and porosity

The surface morphology of the core-shell was examined by Scanning Electron Microscopy (SEM). Samples were dispersed and fixed on sample holders with double-sided adhesive carbon tape (NEM tape; Nisshin, Japan), coated with a 9–12 nm layer of gold/palladium (Polaron, Bad

Table 1
Formulation of core-shell particles prepared via prilling technology: Composition of core and shell components.

Particle name	Core			Shell	
	Alginate (w/v)	Silk fibroin (w/v)	Adenosine (wt. ratio SF:ADO)	Alginate (w/v)	Silk sericin (w/v)
Control	1%	–	–	1.75%	–
SF/ALG + ALG	0.1%	5%	–	1.75%	–
SF/ALG/ADO+ALG	0.1%	5%	5:1	1.75%	–
SF/ALG + ALG/SS	0.1%	5%	–	1.75%	0.09%
SF/ALG/ADO+ALG/SS	0.1%	5%	5:1	1.75%	0.09%

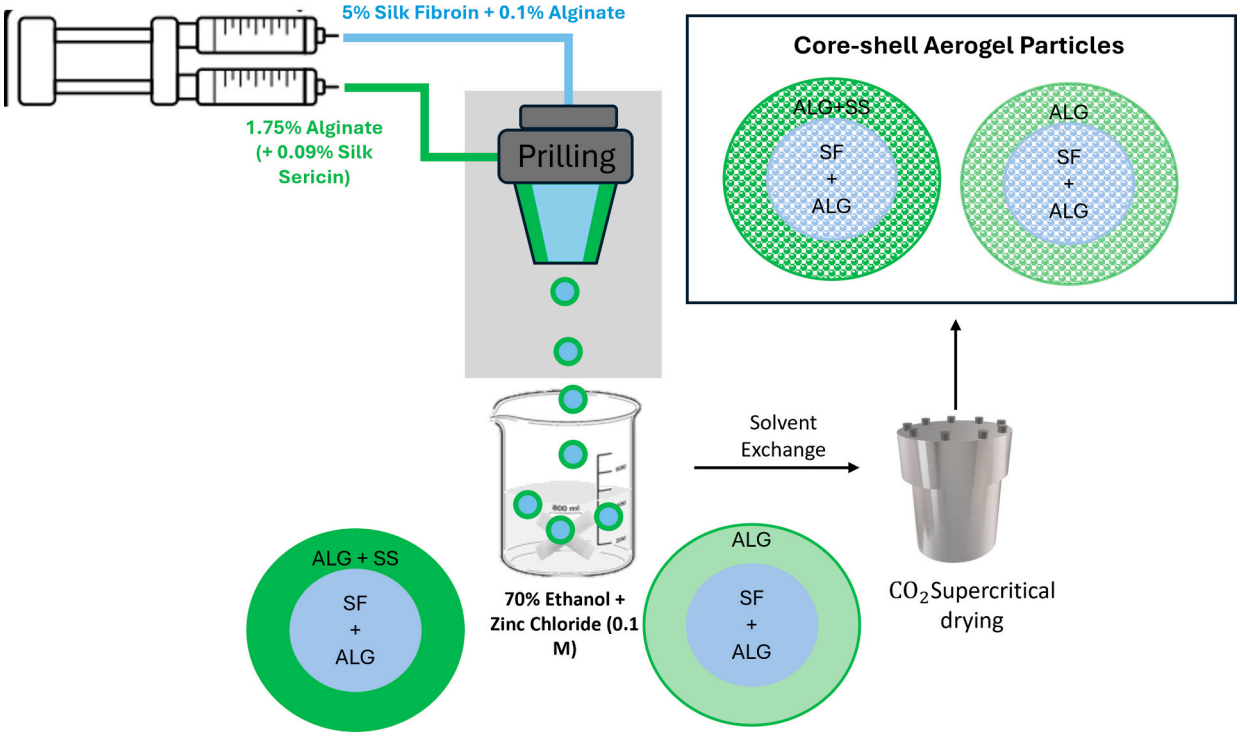

Fig. 1. Schematic representation of the core–shell aerogel particle production process.

Schwalbach, Germany), and analysed using a Phenom Pro G6 SEM (Thermo Fisher Scientific, Eindhoven, Netherlands) at 10 kV with the secondary electron detector (SED).

Shell thickness was measured using an Axiolab optical microscope (Zeiss, Oberkochen, Germany) equipped with an Axiocam 208 color camera (Zeiss, Oberkochen, Germany) at 10× magnification. Around 50 particles were imaged, and measurements were performed using ImageJ (v1.54).

Particle size and distribution were assessed using a Camsizer X2 (Microtrac Retsch GmbH, Haan, Germany) with the X-Dry and X-Fall modules for dry dispersion. This system features dual-laser illumination and high-speed cameras and can analyse particles between 0.8 µm and 8 mm. Measurements were based on 2D projections and evaluated Dv10, Dv50, Dv90, sphericity (0.4–1.0), and convexity (0.98–1.00). Only particles ranging from 0.25 mm to 3.00 mm were considered, and these were grouped into 25 linear size classes. Data analysis was performed using the instrument's built-in software with predefined criteria.

The skeletal density (ρ_{skel}) of the particles was measured by helium pycnometry (MPY-2, Quantachrome, Delray Beach, FL, USA) under controlled conditions (25 °C, 1.03 bar). Envelope density (ρ_{env}) was calculated by dividing the average mass of approximately 50 particles by their estimated mean volume, based on Camsizer-derived diameters and assuming spherical geometry. Total porosity (ε) was then expressed as a percentage and calculated according to Eq. (1).

$$\varepsilon = \left(1 - \frac{\rho_{env}}{\rho_{skel}}\right) \times 100 \quad (1)$$

Textural properties were assessed by Nitrogen adsorption–desorption analysis using an ASAP 2000 system (Micromeritics, Norcross, GA, USA). The specific surface area (aBET) was calculated using the Brunauer–Emmett–Teller (BET) method, while pore size distribution, total pore volume (Vp,BJH), and average pore diameter (Dp, BJH) were obtained via the Barrett–Joyner–Halenda (BJH) method. Specific mesopore volume (V_{mes}) was determined from cumulative BJH data within the 2–50 nm range, and specific macropore volume (V_{mac}) was calculated by subtracting V_{mes} from the total specific pore volume, the latter derived as the inverse of ρ_{env}.

2.4. Spectral data acquisition and analysis

Mid-infrared spectra of the core–shell particles were recorded using a PerkinElmer Spectrum BX FTIR spectrophotometer (Waltham, MA, USA) equipped with a DTGS detector. Measurements were performed in diffuse reflectance mode using a PIKE Technologies Gladi ATR accessory, covering the 4000–600 cm^{-1} range at a resolution of 4 cm^{-1}, with 32 co-added scans per spectrum. Samples were pressed onto the ATR crystal under constant pressure, and the crystal was cleaned between measurements. Three spectra were collected per sample.

Spectral pre-processing and modelling were performed in MATLAB

R2023a (MathWorks, Natick, MA, USA) and PLS Toolbox 9.2.1 (Eigenvector Research, Manson, WA, USA). Preprocessing included standard normal variate (SNV) correction [31] and Savitzky–Golay filtering (15-point smoothing, 2nd-order polynomial, 2nd derivative) [32], followed by mean-centered. Infrared spectra were modelled through a principal component analysis (PCA) [33].

2.5. ADO release and loading capacity evaluation

To assess the release profile of ADO, 15 mg of core–shell particles were suspended in phosphate-buffered saline medium (PBS, pH 7.4) at 5 mg/mL and incubated at 37 °C with constant agitation (100 rpm). At specific time intervals (5, 30 min; 1, 2, 4, 6, and 24 h), 0.5 mL aliquots were collected and replaced with fresh PBS to maintain sink conditions.

For drug loading analysis, 15 mg of particles were incubated in PBS (pH 7.4) at 37 °C for 24 h under agitation to ensure complete ADO release. Loading capacity was calculated in two ways: relative to the total particle mass and relative to the estimated core mass. The core mass was derived from the core-to-shell ratio, using the flow rates during prilling and the initial composition of each formulation. The core accounted for approximately 56.66% (SF/ALG/ADO+ALG) and 55.42% (SF/ALG/ADO+ALG/SS) of the total particle mass. These values enabled accurate estimation of ADO content, specifically within the core. Drug loading and entrapment efficiency were determined using previously described methods [28].

ADO concentrations were determined using High-Performance Liquid Chromatography with Diode Array Detection (HPLC-DAD; Agilent 1260 Infinity II, Agilent Technologies, Santa Clara, CA, USA), following a previously described method [28]. Separation was performed on a ZORBAX Eclipse XBD-C18 column (4.6 × 250 mm, 5 μm; Agilent) using a mobile phase of 10% (v/v) acetonitrile in water, at a flow rate of 0.8 mL/min. Detection was at 260 nm, and quantification was performed using an external ADO calibration curve (0.5–100 μg/mL, $R^2 > 0.995$).

2.6. Swelling tests

Swelling behavior of the core-shell samples (10 mg) was assessed by immersing them in 50 mL of simulated wound fluid (SWF) at pH levels 5.5, 7.4, and 8.5—representing healthy skin, healing wounds, and infected/chronic wound conditions, respectively. [34]. Samples were incubated at 37 °C, and their wet weight (w_t) was recorded at various time intervals (5, 15, 30 min; 1, 2, 4, and 6 h). The swelling ratio was then calculated using Eq. (2).

$$\textit{swelling ratio}\ (\%) = \frac{w_t - w_d}{w_d} \times 100 \quad (2)$$

where w_d corresponds to the initial dry weight of the materials.

2.7. In vitro cell viability and cell behavior

2.7.1. Cell seeding and sample preparation

To assess cell viability and proliferation, HDF, HaCaT, and HDMEC were seeded in 96-well plates at densities of 1.0×10^5, 5.0×10^4, and 2.0×10^4 cells/mL, respectively. For SEM and fluorescence microscopy analysis, HDFs cells were seeded at 5×10^4 cells/mL. Cell density was adjusted according to the proliferation rates of each cell type, with higher seeding for faster-growing HaCaT cells and lower density for HDMECs to avoid contact inhibition [35]. The culture medium for HDF and HaCaT cells was Dulbecco's Modified Eagle's Medium (DMEM; Gibco™ DMEM, high glucose) supplemented with 10% fetal bovine serum (FBS; BioWest) and 1% penicillin-streptomycin (Lonza, Basel, Switzerland). HDMECs were cultured in Endothelial Cell Medium Kit (Innoprot, Derio, Spain). The plates were incubated at 37 °C in a humidified atmosphere with 5% CO_2 for 24 h.

Core-shell aerogel particles were UV-sterilized for 30 min and dispersed in culture medium (1 mg/mL). Leachables were collected at 24, 48, and 72 h to study ADO release, its impact on cell behavior over time, and its stability. Two concentrations (0.25 and 0.1 mg/mL) were tested. Additional assays used 24 h leachables for cell proliferation (both concentrations) and imaging (0.25 mg/mL).

2.7.2. Metabolic activity and cytotoxicity

To assess the metabolic activity and cytotoxicity of leachables from core–shell particles, AlamarBlue assays were conducted using the collected leachables. After 24 h of cell exposure, 100 μL of resazurin solution (0.1 mg/mL) was added, and fluorescence was measured after 2 h (excitation: 530 nm, emission: 590 nm) using a microplate reader (Synergy Mx, Biotek, Santa Clara, CA, USA). Cell proliferation was evaluated using a BrdU incorporation assay (Cell Proliferation ELISA BrdU, colorimetric; Roche Diagnostics, Mannheim, Germany) following standard protocols.

2.7.3. Cell morphology

2.7.3.1. SEM. HDFs, HaCaT, and HDMECs were cultured on TCP coverslips to study cell-material interactions. After leachable exposure, cells were rinsed with PBS and fixed with 2.5% glutaraldehyde for 30 min at room temperature, then stored for analysis. For SEM imaging, samples were dehydrated through graded ethanol and dried with hexamethyldisilazane (HMDS). Samples were mounted on carbon stubs (NEM tape; Nisshin, Japan), sputter-coated with gold/palladium (Polaron, Bad Schwalbach, Germany), and imaged using a Phenom Pro G6 SEM (Thermo Fisher Scientific, Eindhoven, Netherlands) at 5 kV with SED.

2.7.3.2. Fluorescence microscopy. To evaluate cell morphology, samples were stained for filamentous actin (F-actin) and nuclei (DAPI). After fixation with 4% (v/v) formaldehyde and permeabilization with 0.5% (v/v) Triton X-100, non-specific binding was blocked with 5% (v/v) FBS. Imaging was performed using a ZEISS Axio Vert A1 FL inverted microscope (ZEISS, Oberkochen, Germany), with an LED light source and the X-Cite Xylis (D) illumination system. Images were acquired using a ZEISS Axiocam 305 and processed with ZEN Microscopy Software (ZEISS, Oberkochen, Germany).

2.7.4. Anti-inflammatory tests

HaCaT cells were seeded at 1×10^5 cells/mL in 24-well plates and incubated for 24 h. The medium was then replaced with core-shell particle leachables (0.25 mg/mL), with or without 1 μg/mL LPS, and incubated for another 24 h. DEXA (50 nM) served as an anti-inflammatory control. Supernatants were collected, centrifuged, and stored at −20 °C. ELISA was used to quantify Interleukins 1 α (IL-1α) and 6 (IL-6) (ELISA MAX™ Deluxe Set Human IL-1α and ELISA MAX™ Deluxe Set Human IL-6 kit (Biolegend, CA, USA)), respectively. Total protein was measured using RIPA lysis and the Pierce BCA Protein Assay Kit (Thermo Fischer Scientific, Waltham, MA, EUA). Results were normalized by total protein amount.

2.7.5. Chorioallantoic membrane (CAM) assay

The CAM assay was used to assess angiogenesis and biocompatibility of core-shell particles. Fertilized chicken eggs (50–60 g) (Coren, Ourense, Spain) were incubated at 37.8 °C with 60% humidity. On embryonic day 4 (E4), a small window was made in the shell after removing ~2.5 mL of albumin to detach the CAM; the shell was sealed with parafilm and returned to incubation. At E7, particles were applied to the CAM, and after 3 days (E10), the membranes were fixed *in ovo* with 10% formaldehyde (Panreac, Barcelona, Spain) and excised. Controls included untreated eggs.

Images of the inoculation sites were captured *ex ovo* using a stereo microscope (Olympus, B061, Hamburg, Germany), and angiogenesis

was quantified by counting the vessels directed toward the application site.

2.8. Statistical analysis

Quantitative data were subjected to an analysis of variance (one-way ANOVA) followed by a post hoc Tuckey's test or Kruskal-Wallis test, using a level of significance (α) of 0.05. Statistical analyses were performed using GraphPad Prism v. 9.3.1 (GraphPad Software, La Jolla, CA, USA).

3. Results and discussion

3.1. Morphological characterization of core–shell particles

3.1.1. Optical and SEM analysis

The morphology and structural integrity of the core–shell particles were assessed using macroscopic imaging, optical microscopy, and SEM analysis (Fig. 2).

Optical microscopy (Fig. 2B) confirmed the formation of distinct core–shell structures, with a clear interface between the core and shell. SEM images (Fig. 2C) showed spherical particles with aligned surface features. ALG particles appeared smaller and showed shrinkage-related surface changes, while SF/ALG + ALG particles retained their size and displayed lamellar-like topography, likely due to the higher viscosity of the SF core [36]. SF/ALG + ALG/SS particles showed intermediate

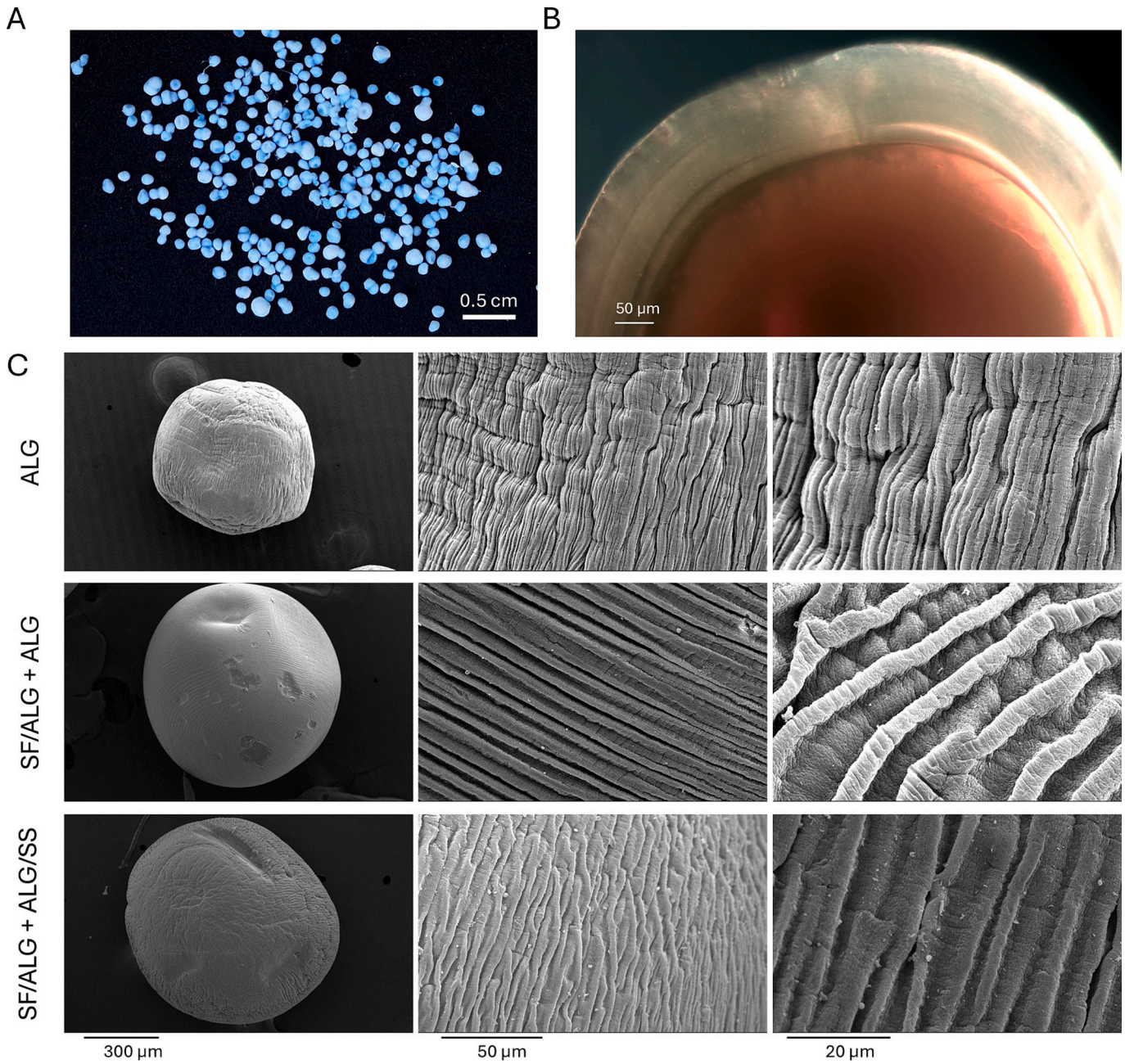

Fig. 2. Morphology of core–shell particles. A. Macroscopic image of a representative core–shell particle; B. optical micrograph of core–shell particles (representative image shown); C. SEM micrographs of core–shell particles composed of ALG, SF/ALG + ALG, and SF/ALG + ALG/SS.

traits, with less uniform surfaces and irregular folding, suggesting the influence of SS in the shell. Interestingly, SS appeared to reduce surface roughness compared to ALG particles, likely due to its film-forming and adhesive properties. This observation aligns with previous findings reporting smoother surfaces when SS is blended with ALG [37].

3.1.2. Particle size, distribution, and shell thickness

Table 2 presents the size-related parameters of the core–shell particles, including mean diameter, distribution (Dv10, Dv50, Dv90), span, and shell thickness. ALG particles showed the smallest and most uniform size. In contrast, formulations with SF or SS had larger and more variable dimensions, with SF/ALG + ALG particles being the largest and most dispersed. These differences likely stem from increased viscosity and altered flow behavior during prilling, affecting droplet formation and stability [36,38].

ALG particles had the thickest shells (100.76 μm), while SF/ALG/ADO+ALG had the thinnest (61.85 μm). The reduced shell thickness in SF- and SS-containing formulations may be linked to their higher viscosity, which enhances encapsulation and interfacial cohesion but can also disrupt uniform droplet formation during prilling [15]. In addition to the effect on shell thickness, the presence of silk proteins (SF or SS) and/or ADO showed increased core volumes (71–76%) compared to the control (54%), suggesting a shift toward core-dominant structures that may improve encapsulation and release performance.

3.2. Chemical analysis

Fig. 3A shows the FTIR spectra for the core–shell particles. Most samples had similar profiles, with the greatest differences observed in ADO-containing particles. The spectra were dominated by characteristic ALG bands at 1600 cm^{-1} (-COO asymmetric stretching); 1405 cm^{-1} (-COO symmetric stretching) and 1080 cm^{-1} (C—O elongation), along with a broad O—H band at 3250 cm^{-1} [39]. An additional band at 3285 cm^{-1}, overlapping with the O—H region and visible in the second derivative spectra (Fig. S1), was detected in all samples except the ALG formulation. This band was attributed to N—H stretching from SF and SS [40].

A PCA was developed using spectra from all particles in the region 1750–800 cm^{-1}. The scores map and the corresponding model loadings are presented in Fig. 2B–C, respectively. The first principal component (PC1), accounting for approximately 77% of the total variance, distinctly separated ADO-containing particles from those without ADO. The most influential wavenumber regions for this separation were 1612–1582 cm^{-1}; 1092–1012 $cm^{-1,}$ and at 880 cm^{-1}. The second component (PC2) further differentiated the non-ADO formulations, with major contributions at 1622 cm^{-1}, 1572 cm^{-1}, 1522 cm^{-1}, and 1492 cm^{-1}. These discriminative regions correspond to prominent absorption bands of the constituent materials, though the spectral complexity of the pure compounds limits precise band assignments. PCA analysis clearly distinguished between ADO-containing and non-ADO particles. Among the non-ADO formulations, SF/ALG + ALG/SS particles were most similar to the ALG control, while SF/ALG + ALG particles were most distinct. This demonstrates the effectiveness of PCA in differentiating between particle compositions based on their spectral profiles.

3.3. Textural characterization

Table 3 summarizes the structural characteristics of the core–shell particles, including ρ_{skel}, ρ_{env}, ε, aBET, and pore volume distribution. ρ_{skel} ranged from 1.36 to 1.56 g/cm^3 with notable differences between ADO-containing and non-ADO samples, suggesting drug incorporation influences ρ_{skel}. Additionally, a notable distinction was observed between the SF/ALG + ALG and SF/ALG + ALG/SS samples, suggesting that the incorporation of SS significantly influences the particles' internal structural properties. Regarding ρ_{env}, it varied notably between SF/ALG + ALG and SF/ALG/ADO+ALG formulations, likely due to a reduction in shell thickness and particle size, which could contributed to the lower ρ_{env} observed.

All formulations showed high porosity (94–97%), typical of aerogels. SF/ALG/ADO+ALG had slightly lower ε, likely due to denser ADO encapsulation. It also had the lowest aBET (272 m^2/g), while SS-containing formulations reached the highest values (451 and 439 m^2/g), suggesting SS enhances pore formation.

Vp,BJH values were higher in SF/ALG + ALG/SS (3.47 cm^3/g) and SF/ALG/ADO+ALG/SS (3.33 cm^3/g), and lower in SF/ALG/ADO+ALG (2.26 cm^3/g). All samples were mainly macroporous, with SF/ALG + ALG showing the greatest macroporosity (16.42 cm^3/g). ADO reduced both meso- and macropore volumes, though SS-containing formulations retained higher mesopore volumes (>3.0 cm^3/g), indicating a predominantly macroporous structure. Taylan et al. [41] developed ALG-based core–shell aerogels with a high specific surface area (337.7 m^2/g) and mesoporosity, demonstrating that increased surface area improves drug adsorption by providing more binding sites. Additionally, larger pore diameters enhance release by reducing diffusion resistance. SF and SS-based core–shell particles show promise for drug delivery, though their macroporosity may lead to faster release.

3.4. Swelling behavior

Swelling studies were conducted at pH 5.5, 7.4, and 8.5 for 6 h to evaluate the pH responsiveness of the core–shell particles (Fig. 4). At physiological pH (7.4), ALG particles showed the highest swelling (~140% within 2 h) (Fig. 4A), maintaining this level throughout. In contrast, other formulations exhibited moderate swelling, stabilizing between 20 and 35% (Fig. 4B).

Under acidic conditions (pH 5.5) (Fig. 4C), swelling was significantly reduced across all samples. SF-ALG and SS-ALG maintained slightly higher values (~30–35%), while both ADO-loaded formulations remained around 20%, indicating a dampening effect of adenosine on swelling capacity. At alkaline pH (8.5) (Fig. 4D), SF/ALG + ALG exhibited a rapid initial swelling (~90% at 1.5 h), followed by a decline likely due to matrix destabilization. In contrast, SF/ALG/ADO+ALG particles maintained a more stable profile (~40%), while other formulations showed signs of degradation. These trends reflect the influence of macroporosity and material composition on fluid uptake. Sellitto et al. also reported a similar behavior in SF/ALG beads, which maintained structural stability for approximately 40 min before showing a gradual decline, likely associated with matrix degradation and partial structural collapse in SWF at 37 °C [26]. In addition to the swelling behavior, the literature indicates that ALG particles undergo faster degradation compared with beads containing SF, consistent with the well-established

Table 2
Particle size distribution analysis of core–shell particles, including Dv10, Dv50, Dv90, span, shell thickness, core, and shell volume.

	Mean diameter (mm)	Dv10 (mm)	Dv50 (mm)	Dv90 (mm)	Span	Shell thickness (μm)	Core volume (%)	Shell volume (%)
ALG	1.06 ± 0.08	0.85 ± 0.04	1.05 ± 0.12	1.29 ± 0.09	0.41 ± 0.01	100.76 ± 25.81	54 ± 10	46 ± 10
SF/ALG + ALG	1.47 ± 0.12	0.99 ± 0.14	1.37 ± 0.30	2.11 ± 0.42	0.81 ± 0.14	70.67 ± 16.19	74 ± 5	26 ± 5
SF/ALG + ALG/SS	1.43 ± 0.12	1.03 ± 0.10	1.35 ± 0.11	1.97 ± 0.18	0.70 ± 0.06	76.68 ± 19.38	71 ± 6	29 ± 6
SF/ALG/ADO+ALG	1.43 ± 0.11	1.03 ± 0.14	1.37 ± 0.13	1.89 ± 0.11	0.63 ± 0.15	61.85 ± 13.67	76 ± 5	24 ± 5
SF/ALG/ADO+ALG/SS	1.38 ± 0.20	0.96 ± 0.12	1.29 ± 0.17	1.98 ± 0.38	0.79 ± 0.13	74.80 ± 19.83	71 ± 7	29 ± 7

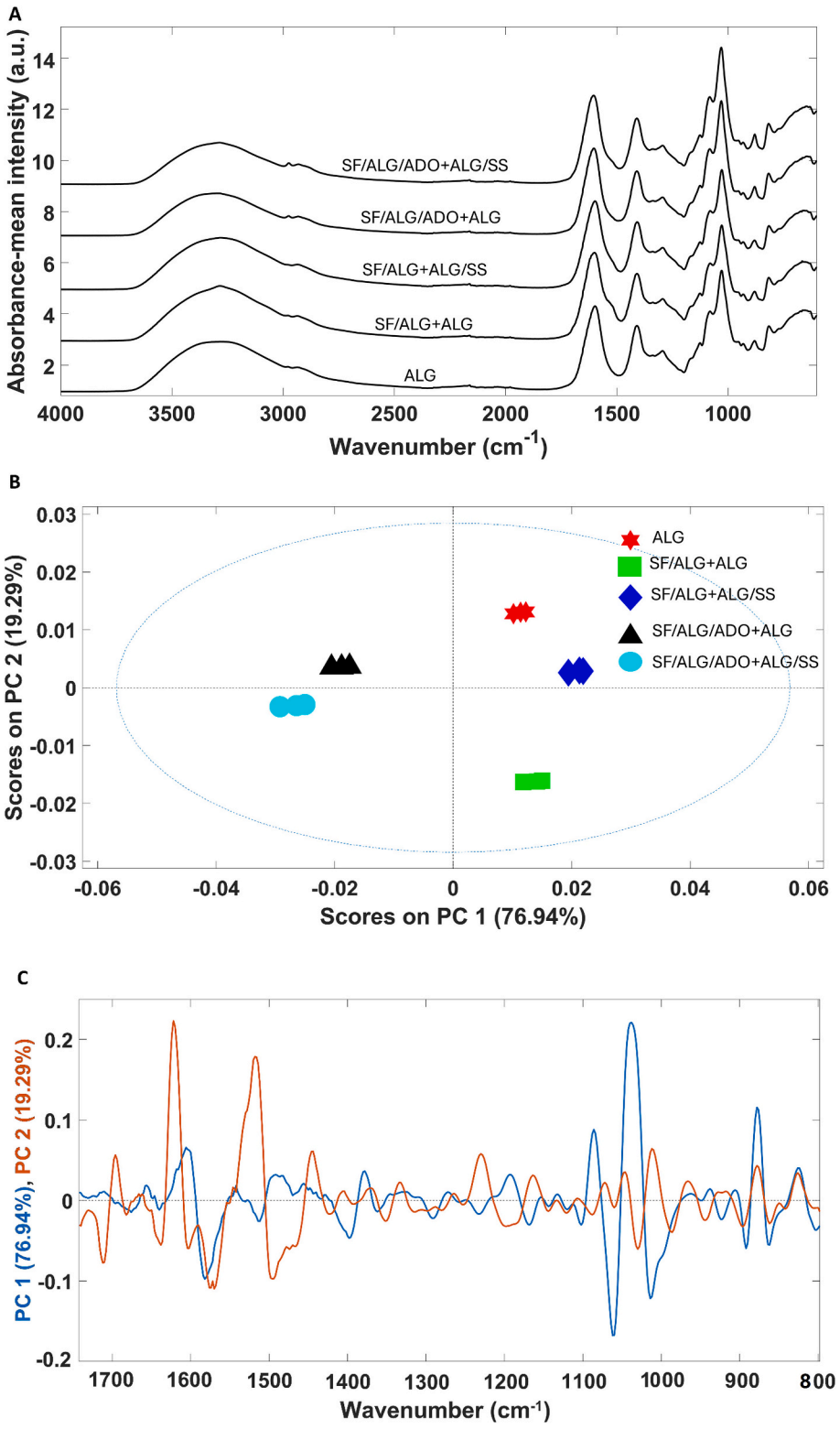

Fig. 3. A. Spectra of the particles included in this study. B. Scores map of the PCA model obtained with infrared spectra of all the particles; C. and the corresponding model loadings.

role of SF in biomaterials, where its superior structural integrity and slower degradation kinetics support prolonged scaffold stability and extended residence times [26]. Similarly, SF aerogel microparticles exhibited a 20–40% degradation during 72 h [29]. Furthermore, SS is also known to be degradable; for example, Baptista-Silva et al. reported that SS undergoes approximately 20% degradation in the presence of physiological proteases after 24 h at 37 °C, reinforcing the expected degradation profile of the polymer components used in this system [42].

The hydrophobic nature and β-sheet structure of SF and SS contribute to limited water absorption, whereas ALG enhances swelling due to its hydrophilic character and gel-forming ability in the presence of divalent cations. As shown in Fig. 4E, swelling of the SF/ALG + ALG

Table 3
Textural properties of the core–shell aerogel particles. Notation: Statistical comparisons were performed across formulations. Identical letters (e.g., a, b) indicate groups that are not significantly different from each other. Comparisons were made between ALG, SF/ALG-ALG, and SF/ALG-ALG/SS formulations; SF/ALG-ALG and SF/ALG/ADO-ALG; and SF/ALG-ALG/SS and SF/ALG/ADO-ALG/SS.

Particles	ρ_{skel} (g/cm^3)	ρ_{env} (g/cm^3)	ε (%)	aBET (m^2/g)	Vp,BJH (cm^3/g)	Dp,BJH (nm)	V_{mes} (cm^3/g)	V_{mac} (cm^3/g)
ALG	1.54 ± 0.03^a	0.06 ± 0.01^a	96 ± 0.50	377 ± 19	2.99 ± 0.15	29.53 ± 1.48	2.75 ± 0.14	13.18 ± 0.70
SF/ALG + ALG	1.56 ± 0.03^a	0.05 ± 0.01^a	97 ± 0.60	412 ± 21	3.22 ± 0.16	27.11 ± 1.36	2.98 ± 0.15	16.42 ± 1.11
SF/ALG + ALG/SS	1.39 ± 0.02^b	0.07 ± 0.01^a	95 ± 1.03	439 ± 22	3.47 ± 0.17	27.57 ± 1.38	3.15 ± 0.16	13.60 ± 1.53
SF/ALG/ADO+ALG	1.36 ± 0.02^b	0.08 ± 0.01^b	94 ± 0.84	272 ± 14	2.26 ± 0.11	27.38 ± 1.37	2.09 ± 0.10	9.70 ± 1.05
SF/ALG/ADO+ALG/SS	1.50 ± 0.04^a	0.07 ± 0.01^a	95 ± 0.96	451 ± 23	3.33 ± 0.17	26.03 ± 1.30	3.03 ± 0.15	10.37 ± 2.23

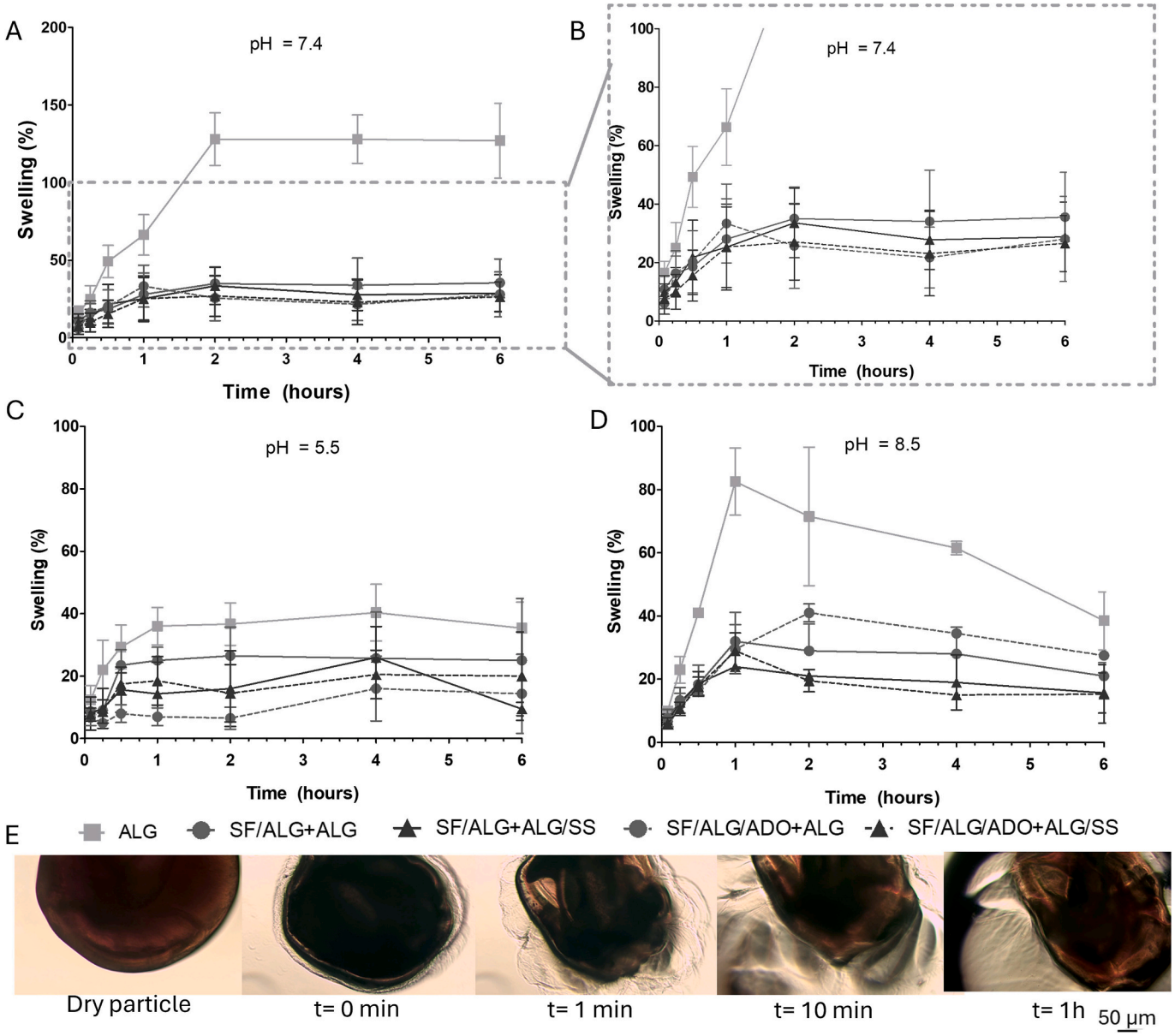

Fig. 4. Swelling behavior of core–shell particles under different pH conditions monitored over 6 h ($n = 3$): A. pH 7.4 (y-axis up to 200%); B. pH 7.4; C. pH 5.5; and D. pH 8.5; E. optical microscopy images showing the time-dependent swelling behavior of SF/ALG + ALG particles, at pH = 7.4 during 1 h.

particles occurs predominantly in the outer shell, confirming this enhancing effect. This property supports exudate management and promotes a moist environment favorable for tissue regeneration, making ALG a valuable component in wound healing applications [43]. This helps to maintain a moist wound environment, which is key for effective healing as it supports tissue regeneration, facilitates exudate control, and minimises the risk of maceration.

3.5. Drug release profile, loading and entrapment yield

To determine ADO incorporation within the core–shell systems, a quantitative analysis of drug loading, core-specific loading, and entrapment efficiency was conducted (Table 4). Both SF/ALG/ADO-+ALG and SF/ALG/ADO+ALG/SS formulations effectively encapsulated ADO, with the former exhibiting higher drug content, loading

Table 4
ADO content, loading, core loading, and encapsulation parameters for SF/ALG/ADO+ALG and SF/ALG/ADO+ALG/SS core–shell particles.

Particles	ADO total mass[a] (μg)	Loading (%)	Core loading (%)	Entrapment yield (%)
SF/ALG/ADO+ALG	203.92 ± 13.43	1.36 ± 0.09	2.40 ± 0.16	6.80 ± 0.45
SF/ALG/ADO+ALG/SS	146.96 ± 4.99	0.98 ± 0.03	1.77 ± 0.06	4.90 ± 0.17

[a] In 15 mg of core-shell particles.

capacity, and entrapment yield. Although overall loading efficiencies were moderate, the detectable presence of ADO confirms the effectiveness of the encapsulation strategy.

The encapsulation performance was reflected in the release profiles (Fig. 5), which showed an initial burst followed by a plateau for both SF/ALG/ADO+ALG and SF/ALG/ADO+ALG/SS. The SS-containing formulation exhibited a faster initial release, likely due to enhanced ADO diffusion facilitated by SS's solubility. Despite this, SF/ALG/ADO+ALG released a higher amount of ADO, consistent with its higher drug loading and core volume. These results underscore the influence of formulation composition and structural design on both encapsulation efficiency and release kinetics.

Encapsulation efficiency and drug loading are highly dependent on material properties and fabrication techniques. For instance, PVA-core/SF-shell nanoparticles have achieved over 90% efficiency for Doxorubicin (DOX) [44], with the PVA/SF ratio influencing release behavior. While the SF shell mitigated burst release, substantial drug retention occurred within the carrier. These results surpass those of the current system, which can be attributed to differences in drug hydrophobicity (DOX vs. ADO), core material (PVA vs. SF), particle size, and production method (electrospraying vs. prilling). Although ADO is predominantly hydrophilic, its hydrophobic regions may interact with non-polar SF amino acids such as alanine and glycine [45–47].

Additionally, Taylan et al. [41], demonstrated that ALG-based core–shell aerogels (1.5% core, 2.0% shell) achieved a drug loading of 5.9%, outperforming conventional aerogels (2.3–3.4%). Despite slightly higher values, the differences remain modest considering the variation in materials, techniques, and drug types. More recently, Illanes-Bordomás et al. [10], reported further moderate loading for vancomycin, but significant drug loss occurred during alcogel formation and supercritical drying [10]. Dexamethasone exhibited very low loading due to poor matrix retention and ethanol solubility. These findings emphasize the importance of optimizing loading strategies, including reducing solvent exposure and tailoring crosslinking or post-drying methods. SF/ALG aerogel beads loaded with ciprofloxacin, 2% and 5% formulations showed similar initial release profiles, although higher loading led to faster early diffusion due to increased concentration gradients and unbound drug [26]. Kinetic analysis indicated a Weibull profile and non-Fickian (Korsmeyer–Peppas) behavior, reflecting a combined mechanism of diffusion and matrix relaxation or erosion.

In core–shell systems with SF-based cores, such as curcumin-loaded electrospun fibers, the hydrophobic nature of the drug and extended diffusion path contribute to slower release, despite a minor initial burst [23]. Translating this to ADO-loaded particles, the hydrophilic nature of ADO and its core localization may similarly influence delayed or incomplete release. These insights suggest that modifying the shell composition (e.g., incorporating SF) could be a viable strategy for better regulating release kinetics and mitigating the initial burst. Silva et al. [48], reported that single-polymer microparticles released ciprofloxacin and curcumin rapidly (≈80% in 10 h), whereas in the core–shell design, ciprofloxacin in the outer layer showed similarly fast release but curcumin confined to the core diffused much more slowly—only ~50% in 24 h and requiring 15 days for full release—demonstrating how the core–shell structure provides a diffusion barrier that reduces burst release and enables sustained delivery.

Overall, these studies show that core–shell systems typically achieve modest encapsulation and faster release for small, hydrophilic drugs, while hydrophobic molecules such as curcumin exhibit slower, sustained diffusion when confined in a core due to their low solubility and stronger interactions with the matrix; thus, the low ADO loading and its rapid release observed in our particles are consistent with published trends, and modifying the shell composition—such as incorporating silk fibroin to increase drug–matrix affinity—may help improve retention and release control.

3.6. *In vitro biological evaluation*

Fig. 6A–F presents cell viability at 24, 48, and 72 h following exposure to particle leachables collected after 24 h of release.

Cell viability results (Fig. 6A–F) confirmed that all formulations remained well above the cytotoxic threshold (70%) across 24, 48, and 72 h, indicating no adverse effects from particle leachables. In HDF cells

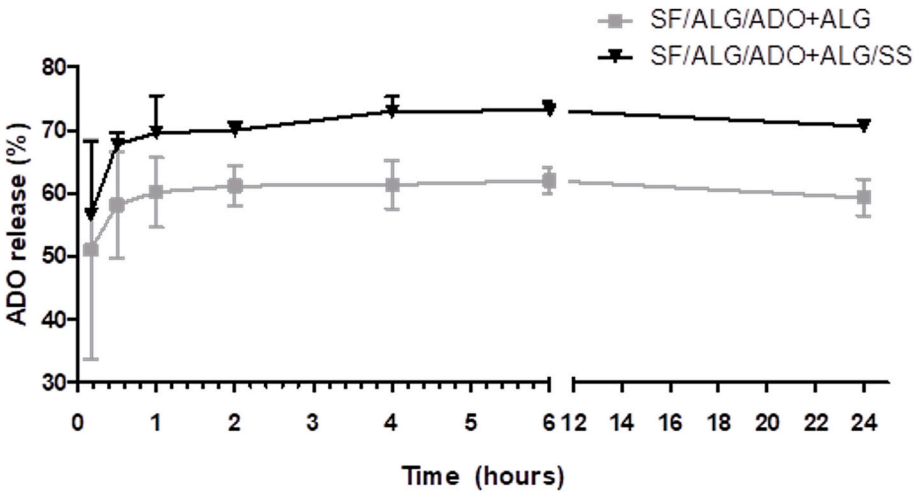

Fig. 5. ADO release profiles from SF/ALG/ADO+ALG and SF/ALG/ADO+ALG/SS core–shell particles over time in PBS at pH 7.4, 37 °C, under continuous agitation at 100 rpm ($n = 3$).

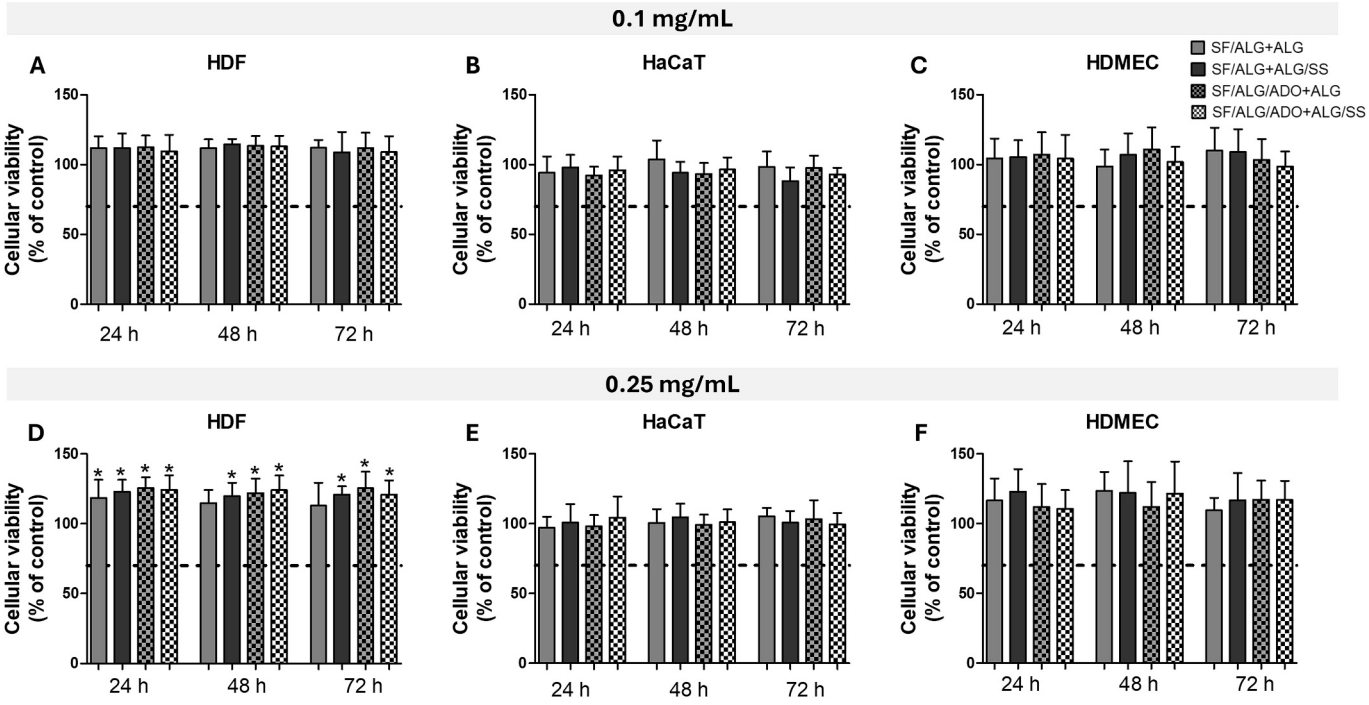

Fig. 6. Cell viability after 24 h exposure to particle leachables collected at 24, 48, and 72 h, corresponding to core–shell particle exposure times in cell culture medium. Panels: (A, D) HDF cells, (B, E) HaCaT cells, and (C, F) HDMEC cells, tested at particle concentrations of 0.1 mg/mL (A–C) and 0.25 mg/mL (D–F), respectively. ($n = 3$) *The differences from the negative control (cell growth) at each time-point were significant at $\alpha < 0.05$.

(Fig. 6D), significant differences were observed among formulations at 24 h, persisting at later time points except for SF/ALG + ALG at 72 h, which aligned with the control. Despite statistical variation, all values remained within biocompatible limits. ADO presence did not compromise viability and even showed a slight enhancement in HDF cells.

To investigate the proliferative potential of the formulations (Fig. 7A), BrdU incorporation was measured at 0.1 and 0.25 mg/mL. HaCaT cells showed the strongest response, with SF/ALG + ALG and SF/ALG + ALG/SS significantly enhancing proliferation at the lower concentration. However, at 0.25 mg/mL, a reduction in BrdU incorporation was observed, indicating a concentration-dependent effect. In contrast, HDF and HDMEC cells did not show statistically significant differences between groups. However, non-significant trends suggest that SS-containing formulations (SS-ALG and SS-ADO) slightly promoted proliferation at the higher concentration. Additionally, particles containing ADO tended to enhance BrdU incorporation, particularly at 0.1 mg/mL, suggesting a potentially favorable role for ADO in supporting cell growth. Though these effects were not statistically significant, they point to promising bioactivity worth further investigation. HDF and HDMEC cells (Fig. 7A) showed no statistically significant differences between groups, though SS-containing formulations (SF/ALG + ALG/SS and SF/ALG/ADO+ALG/SS) exhibited non-significant trends toward enhanced proliferation at 0.25 mg/mL. ADO-containing particles also tended to increase BrdU incorporation at 0.1 mg/mL, at HDF, suggesting a potential role in promoting cell growth.

Core–shell systems offer advantages for wound healing by enabling controlled drug release and enhancing cellular responses. For instance, SS–ALG core microcapsules with chitosan shells enhanced hepatocyte viability in comparison to ALG-only systems, presumably attributable to SS's supportive function in cell proliferation [49]. Similarly, chitosan–calcium ALG microspheres enhanced hemostasis via calcium ion release, demonstrating how shell composition can be tailored to address specific wound healing phases [50].

Cell morphology and cytoskeletal organization were evaluated via fluorescence microscopy and SEM following exposure to ALG, SF/ALG/ADO+ALG, and SF/ALG/ADO+ALG/SS leachables (Fig. 7B) and to all particles leachables (Figs. S2 and S3). SEM imaging (Fig. 7B) confirmed distinct cell-type-specific morphologies: HDFs displayed elongated, spindle-like shapes with extensive substrate coverage; HaCaT cells formed cohesive epithelial layers; and HDMECs showed dynamic spreading and adhesion, consistent with their initial seeding density. ADO-containing formulations appeared to slightly enhance cell density, suggesting a potential stimulatory effect. Fluorescence microscopy (Fig. 7B) revealed well-organized F-actin structures across all cell types, with intact nuclei confirmed by DAPI staining. Minor variations in staining patterns likely reflect inherent cellular differences rather than treatment effects. Both imaging techniques confirmed that cell morphology and cytoskeletal integrity were preserved across all cell types, reinforcing the biocompatibility of the particle formulations.

3.7. *In vitro anti-inflammatory tests*

Anti-inflammatory assays demonstrated that core–shell particles effectively suppressed IL-1α and IL-6 expression (Fig. 7C), with ADO-loaded formulations showing enhanced inhibition. All tested formulations with ADO resulted in lower IL-1α levels than the inflammation control. Moreover, IL-6 concentrations in the ADO-loaded group were comparable to those in the DEXA-treated control, highlighting the strong anti-inflammatory efficacy of ADO. Notably, even unloaded particles reduced cytokine levels, suggesting intrinsic anti-inflammatory properties of SF [3,51]. ADO significantly enhances the suppression of LPS-induced inflammation, showing marked differences compared to controls. This effect is largely attributed to its ability to downregulate the release of major pro-inflammatory cytokines, such as IL-1α and IL-6, primarily through the engagement of A_{2A} and A_{2B} receptors expressed on immune cells [52,53].

3.8. *In ovo chorioallantoic membrane assay*

The angiogenic response toward the core–shell particles was assessed *in ovo* (Fig. 8). Although differences between groups were not statistically significant, a greater number of blood vessels was observed in the

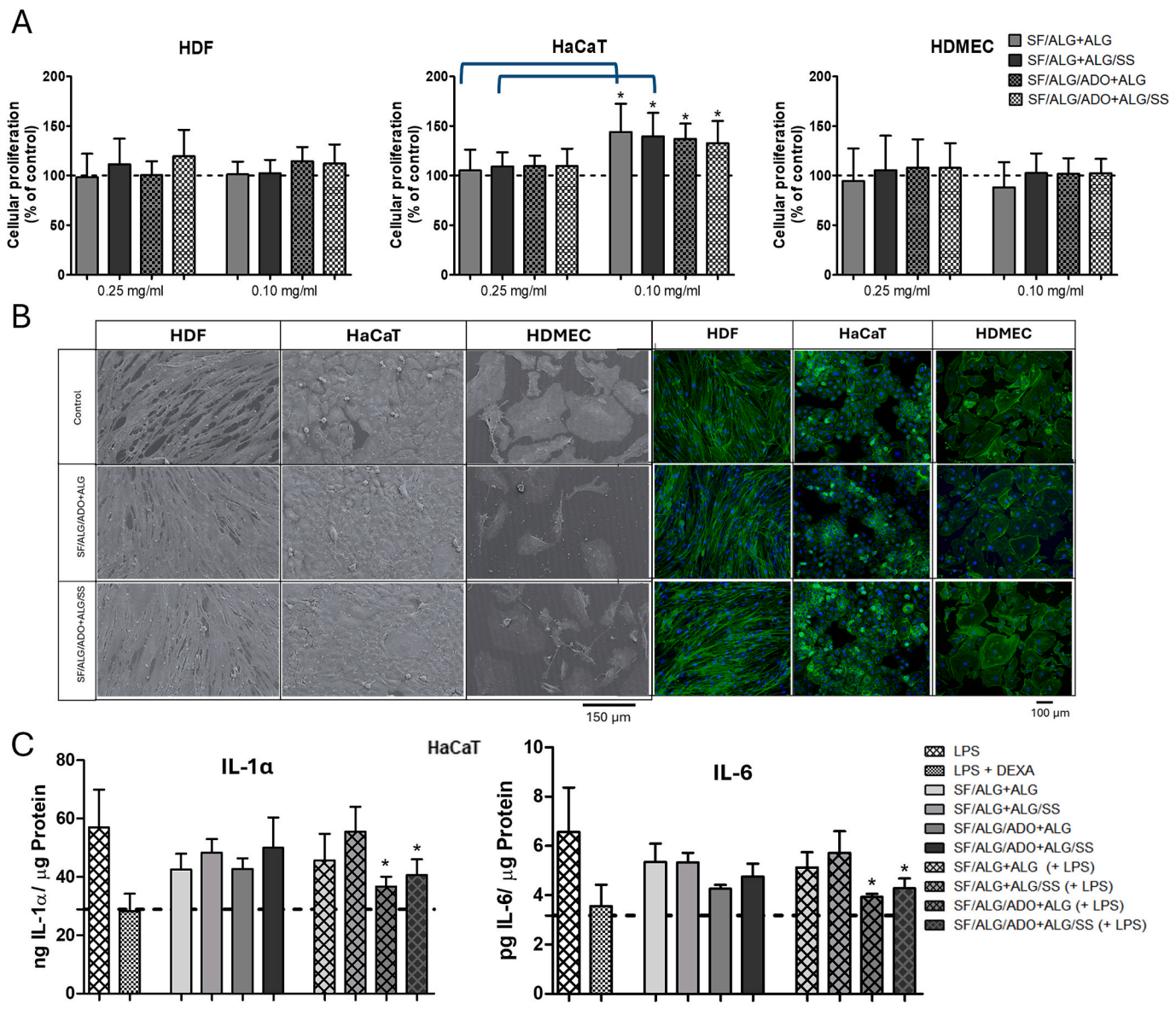

Fig. 7. A. Cell proliferation after 24 h exposure to particle leachables. HDF cells, HaCaT cells, and HDMEC cells were tested at particle concentrations of 0.1 mg/mL and 0.25 mg/mL. ($n = 3$) *The differences from the negative control (cell growth) of each time-point were significant at $\alpha < 0.05$; B. SEM and fluorescence microscopy (cells were stained with phalloidin (green) for F-actin and DAPI (blue) for nuclei) images of HDF, HaCaT, and HDMEC cells after 24 h particle exposure to leachables of ALG, SF/ALG/ADO+ALG and SF/ALG/ADO+ALG/SS at a concentration of 0.25 mg/mL; C. anti-inflammatory activity on HaCaT of core-shell particles assessed by inhibition of pro-inflammatory cytokines in LPS-induced inflammation: IL-1α and IL-6 (n = 3). Notation: Dashed line represents the cells only group (control); LPS – Cells with LPS (inflammatory control); LPS + DEXA – Cells with LPS and DEXA (anti-inflammatory control); the other are the core-shell particles without (e.g., SF/ALG + ALG) and with LPS (e.g., SF/ALG + ALG + LPS). *The differences from the LPS control with core-shell particles with LPS were significant at $\alpha < 0.05$.

presence of ADO compared to unloaded particles. This trend supports the pro-angiogenic role of ADO [54].

Silk-based biomaterials, such as SS hydrogels and SF composites, have shown promise in promoting angiogenesis without triggering inflammation [42,55–57]. Ribeiro et al. [55] reported that SF–polyethylene terephthalate (PET) textile composites promoted significantly more blood vessel formation than PET-only textiles and gelatin sponges. Similarly, Heimes et al. [56] found that SF-based matrices—including hydrated SF with NaCl, SF with enamel matrix protein, and platelet-rich fibrin—induced greater vascularization than collagen scaffolds. Watchararot et al. [57] also observed increased vessel formation and no irritation with SF hydrogels, with mupirocin further enhancing this effect, confirming their strong pro-angiogenic and biocompatible potential.

ADO's pro-angiogenic effects were also confirmed using its analogue ethylcarboxamidoadenosine (NECA), which upregulated VEGF, IL-8, and bFGF via A_2B receptor activation [58]. Additionally, ATP-conjugated selenium nanoparticles showed no toxicity in CAM assays, supporting the safety of ADO-related compounds [59].

4. Conclusion

This study reports, for the first time, the development of SF-based core–shell aerogel particles for controlled drug delivery and tissue regeneration. The combination of SF and SS influenced particle morphology, promoting textured surfaces and improved core–shell structure. Physicochemical analysis confirmed high porosity and structural integrity, while pH-responsive swelling supported their suitability

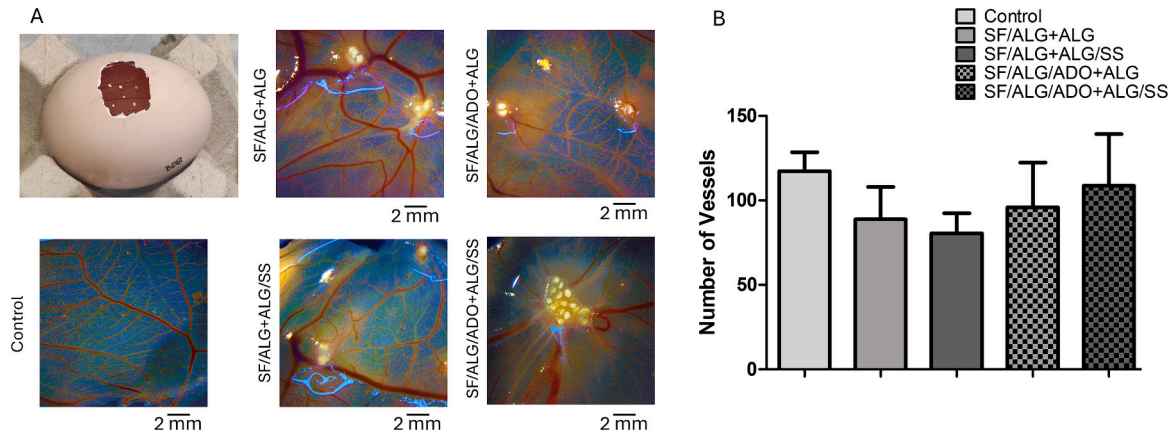

Fig. 8. CAM Assay. (A) Representative image of the fertilized egg and corresponding stereomicroscopic images of the CAM at the inoculation site. (B) Quantitative analysis of blood vessel formation at the site of particle application. The control group consisted of eggs with no material applied ($n = 4$). No statistically significant differences were observed between groups.

for controlled ADO release in complex wound environments. Although encapsulation and loading efficiencies were moderate, the particles demonstrated promising characteristics for sustained ADO delivery, with release profiles modulated by shell composition. In vitro assays using HDF, HaCaT, and HDMEC confirmed biocompatibility, with ADO- and SS-containing particles enhancing cell viability, proliferation, and anti-inflammatory responses. Furthermore, angiogenic potential was supported by the CAM assay. To protect thermolabile ADO and SF from degradation, core-shell particles were fabricated under mild conditions (40 °C), thereby avoiding the thermal damage commonly associated with conventional spray drying. Biological assays demonstrated preserved anti-inflammatory and angiogenic activity. These findings highlight the system's promise for delivering bioactive agents in wound healing, with tunable properties and compatibility for sensitive compounds.

Overall, future work should focus on validating these SF-based core–shell aerogel particles in vivo and improving their encapsulation efficiency, potentially through alternative core–shell configurations, while also addressing current challenges by optimizing crosslinking conditions, tailoring aerogel porosity, and developing scalable fabrication strategies to enhance their controlled delivery of ADO and accelerate their translation as an effective therapeutic platform for chronic wound treatment.

CRediT authorship contribution statement

Beatriz G. Bernardes: Writing – review & editing, Writing – original draft, Visualization, Validation, Methodology, Investigation, Formal analysis, Data curation. **Clara Sousa:** Writing – review & editing, Writing – original draft, Methodology, Data curation. **Maria Rosaria Sellitto:** Writing – review & editing, Methodology, Investigation. **Ana Iglesias-Mejuto:** Writing – review & editing, Methodology, Investigation. **Pasquale Del Gaudio:** Writing – review & editing, Resources. **Raquel Costa:** Writing – review & editing, Supervision, Methodology, Conceptualization. **Carlos A. García-González:** Writing – review & editing, Supervision, Resources, Funding acquisition, Conceptualization. **Ana Leite Oliveira:** Writing – review & editing, Supervision, Resources, Funding acquisition, Conceptualization.

Declaration of competing interest

The authors declare that they have no known competing financial interests or personal relationships that could have appeared to influence the work reported in this paper.

Acknowledgements

This work was supported by National Funds from FCT - Fundação para a Ciência e a Tecnologia through project UID/50016/2025. Work supported by IBEROS+ (0072_IBEROS_MAIS_1_E) - Instituto de Biofabricación en Red para El Envejecimiento Saludable, funded by "Interreg VI A España – Portugal (POCTEP) 2021-2027"; by MICINN [PID2023-151340OB-I00], Agencia Estatal de Investigación [AEI], FEDER funds and Be@t-Textile Bioeconomy (TC-C12-i01, Sustainable Bioeconomy No. 02/C12-i01.01/2022), promoted by the Recovery and Resilience Program (RRP), Next Generation EU, 2021-2026. B.G.B. acknowledges FCT for the Doctoral Research Grant 2021.05717.BD. A. I.-M. acknowledges Xunta de Galicia for her postdoctoral fellowship [ED481B-2025/032] and to FCT for project UID/04138/2025. This publication is based on work from ECO-AERoGELS Innovators Grant (ref. IG18125) supported by COST (European Cooperation in Science and Technology). C.S. thanks to FCT through the contract Nº 2023.15056.TENURE.046.

Appendix A. Supplementary data

Supplementary data to this article can be found online at https://doi.org/10.1016/j.bioadv.2026.214889.

Data availability

Data will be made available on request.

References

[1] T. Lehmann, A.E. Vaughn, S. Seal, K.W. Liechty, C. Zgheib, Silk fibroin-based therapeutics for impaired wound healing, Pharmaceutics 14 (2022) 651, https://doi.org/10.3390/pharmaceutics14030651.
[2] B.G. Bernardes, P. Del Gaudio, P. Alves, R. Costa, C.A. García-González, A. L. Oliveira, Bioaerogels: promising nanostructured materials in fluid management, healing and regeneration of wounds, Molecules 26 (2021) 3834, https://doi.org/10.3390/molecules26133834.
[3] B.G. Bernardes, A. Veiga, J. Barros, C.A. García-González, A.L. Oliveira, Sustainable silk-based particulate systems for the controlled release of pharmaceuticals and bioactive agents in wound healing and skin regeneration, Int. J. Mol. Sci. 25 (2024) 3133, https://doi.org/10.3390/ijms25063133.
[4] G. Kaur, G. Narayanan, D. Garg, A. Sachdev, I. Matai, Biomaterials-based regenerative strategies for skin tissue wound healing, ACS Appl. Bio Mater. 5 (2022) 2069–2106, https://doi.org/10.1021/acsabm.2c00035.
[5] J. Dorogin, J.M. Townsend, M.H. Hettiaratchi, Biomaterials for protein delivery for complex tissue healing responses, Biomater. Sci. 9 (2021) 2339–2361, https://doi.org/10.1039/D0BM01804J.
[6] H. Fan, B. Xue, J. Lu, T. Sun, Q. Zhao, Y. Liu, et al., Recent advances of bioaerogels in medicine: preparation, property and application, Int. J. Biol. Macromol. 291 (2025) 139144, https://doi.org/10.1016/j.ijbiomac.2024.139144.

[7] M.A.S. Abourehab, R.R. Rajendran, A. Singh, S. Pramanik, P. Shrivastav, M. J. Ansari, et al., Alginate as a promising biopolymer in drug delivery and wound healing: a review of the state-of-the-art, Int. J. Mol. Sci. 23 (2022) 9035, https://doi.org/10.3390/ijms23169035.
[8] B. Aderibigbe, B. Buyana, Alginate in wound dressings, Pharmaceutics 10 (2018) 42, https://doi.org/10.3390/pharmaceutics10020042.
[9] M. Kurakula, G.K. Rao, V. Kiran, M.S. Hasnain, A.K. Nayak, Alginate-based hydrogel systems for drug releasing in wound healing, in: Alginates in Drug Delivery, Elsevier, 2020, pp. 323–358, https://doi.org/10.1016/B978-0-12-817640-5.00013-3.
[10] C. Illanes-Bordomás, M. Landin, C.A. García-González, Novel core–shell aerogel formulation for drug delivery based on alginate and konjac glucomannan: rational design using artificial intelligence tools, Polymers (Basel) 17 (2025) 1919, https://doi.org/10.3390/polym17141919.
[11] R. Jenjob, T. Phakkeeree, D. Crespy, Core–shell particles for drug-delivery, bioimaging, sensing, and tissue engineering, Biomater. Sci. 8 (2020) 2756–2770, https://doi.org/10.1039/C9BM01872G.
[12] S.M. Gomes, C. Illanes-Bordomás, C.A. García-González, I.S. Akgün, Engineering aerogel particles as next-generation drug delivery systems: a comprehensive review of recent advances, Int. J. Pharm. 694 (2026) 126722, https://doi.org/10.1016/j.ijpharm.2026.126722.
[13] C. He, X. Lin, L. Shang, Multi-functional responsive microcapsules with sequential release capacity for wound healing, Small 21 (2025) 2410844, https://doi.org/10.1002/smll.202410844.
[14] B. Wen, D. Huang, C. Song, Y. Chen, Y. Zhao, Ultrasound-responsive microcapsules delivering oxygen and traditional Chinese medicine for wound healing, Smart Med. 4 (2025) e70021, https://doi.org/10.1002/smmd.70021.
[15] R. Rodríguez-Dorado, M. Landín, A. Altai, P. Russo, R.P. Aquino, P. Del Gaudio, A novel method for the production of core-shell microparticles by inverse gelation optimized with artificial intelligent tools, Int. J. Pharm. 538 (2018) 97–104, https://doi.org/10.1016/j.ijpharm.2018.01.023.
[16] F. De Cicco, P. Russo, E. Reverchon, C.A. García-González, R.P. Aquino, P. Del Gaudio, Prilling and supercritical drying: a successful duo to produce core-shell polysaccharide aerogel beads for wound healing, Carbohydr. Polym. 147 (2016) 482–489, https://doi.org/10.1016/j.carbpol.2016.04.031.
[17] Y. Fang, X. Zhu, N. Wang, X. Zhang, D. Yang, J. Nie, et al., Biodegradable core-shell electrospun nanofibers based on PLA and γ-PGA for wound healing, Eur. Polym. J. 116 (2019) 30–37, https://doi.org/10.1016/j.eurpolymj.2019.03.050.
[18] Y. Wei, A. Guo, Z. Liu, L. Mao, F. Yuan, Y. Gao, et al., Structural design of zein-cellulose nanocrystals core–shell microparticles for delivery of curcumin, Food Chem. 357 (2021) 129849, https://doi.org/10.1016/j.foodchem.2021.129849.
[19] Z. Li, S. Mei, Y. Dong, F. She, P. Li, Y. Li, et al., Multi-functional core-shell nanofibers for wound healing, Nanomaterials 11 (2021) 1546, https://doi.org/10.3390/nano11061546.
[20] J. Hou, J. Jie, X. Wei, X. Shen, Q. Zhao, X. Chai, et al., A core-shell-type nanosystem promotes diabetic wound healing through photothermal-responsive release of transforming growth factor β, J. Nanobiotechnol. 22 (2024) 449, https://doi.org/10.1186/s12951-024-02675-2.
[21] M.R. Zare, M. Khorram, S. Barzegar, F. Asadian, Z. Zareshahrabadi, M.J. Saharkhiz, et al., Antimicrobial core–shell electrospun nanofibers containing Ajwain essential oil for accelerating infected wound healing, Int. J. Pharm. 603 (2021) 120698, https://doi.org/10.1016/j.ijpharm.2021.120698.
[22] W. Song, M. Muthana, J. Mukherjee, R.J. Falconer, C.A. Biggs, X. Zhao, Magnetic-silk core–shell nanoparticles as potential carriers for targeted delivery of curcumin into human breast cancer cells, ACS Biomater. Sci. Eng. 3 (2017) 1027–1038, https://doi.org/10.1021/acsbiomaterials.7b00153.
[23] M.S. Razavi, P. Ebrahimnejad, H.A. Javar, T.A. Weppelmann, J. Akbari, F.A. Amoli, et al., Development of dual-functional core-shell electrospun mats with controlled release of anti-inflammatory and anti-bacterial agents for the treatment of corneal alkali burn injuries, Biomater. Adv. 154 (2023) 213648, https://doi.org/10.1016/j.bioadv.2023.213648.
[24] Y. Xia, X. Lu, H. Zhu, Natural silk fibroin/polyaniline (core/shell) coaxial fiber: fabrication and application for cell proliferation, Compos. Sci. Technol. 77 (2013) 37–41, https://doi.org/10.1016/j.compscitech.2013.01.008.
[25] Z. Wang, X. Song, Y. Cui, K. Cheng, X. Tian, M. Dong, et al., Silk fibroin H-fibroin/poly(ε-caprolactone) core-shell nanofibers with enhanced mechanical property and long-term drug release, J. Colloid Interface Sci. 593 (2021) 142–151, https://doi.org/10.1016/j.jcis.2021.02.099.
[26] M.R. Sellitto, D. Larobina, C. De Soricellis, C. Amante, G. Falcone, P. Russo, et al., Silk fibroin–alginate aerogel beads produced by supercritical CO2 drying: a dual-function conformable and haemostatic dressing, Gels 11 (2025) 603, https://doi.org/10.3390/gels11080603.
[27] D.S. Mansuroglu, A. Çınarlı, G. Çaylı, D. Gurbuz, Electrospinning of core shell nanofibers using amine modified sericins, Sci. Rep. 15 (2025) 42836, https://doi.org/10.1038/s41598-025-08984-2.
[28] B.G. Bernardes, R. Laurano, C. López-Iglesias, R. Magalhães, R. Costa, C.A. García-González, et al., Silk fibroin microparticles as a candidate for wound healing applications: evaluating the role of adenosine, Int. J. Pharm. 682 (2025) 125930, https://doi.org/10.1016/j.ijpharm.2025.125930.
[29] B.G. Bernardes, S. Baptista-Silva, C. Illanes-Bordomás, R. Magalhães, J.R. Dias, N. M.F. Alves, et al., Expanding the potential of self-assembled silk fibroin as aerogel particles for tissue regeneration, Pharmaceutics 15 (2023) 2605, https://doi.org/10.3390/pharmaceutics15112605.
[30] A. Veiga, R.A. Ramírez-Jiménez, V. Santos-Rosales, C.A. García-González, M. R. Aguilar, L. Rojo, et al., Innovative processing and sterilization techniques to unlock the potential of silk sericin for biomedical applications, Gels 11 (2025) 114, https://doi.org/10.3390/gels11020114.
[31] T. Næs, T. Isaksson, T. Fearn, T. Davies. A User-friendly Guide to Multivariate Calibration and Classification, NIR Publications, Chichester (UK), 2002, https://doi.org/10.1255/978-1-906715-25-0.
[32] Abraham Savitzky, M.J.E. Golay, Smoothing and differentiation of data by simplified least squares procedures, Anal. Chem. 36 (1964) 1627–1639, https://doi.org/10.1021/ac60214a047.
[33] I.T. Jolliffe, Principal Component Analysis, Springer New York, New York, NY, 1986, https://doi.org/10.1007/978-1-4757-1904-8.
[34] L.A. Wallace, L. Gwynne, T. Jenkins, Challenges and opportunities of pH in chronic wounds, Ther. Deliv. 10 (2019) 719–735, https://doi.org/10.4155/tde-2019-0066.
[35] R.M. Marks, M. Czerniecki, R. Penny, Human dermal microvascular endothelial cells: an improved method for tissue culture and a description of some singular properties in culture, In Vitro Cell. Dev. Biol. 21 (1985) 627–635, https://doi.org/10.1007/BF02623295.
[36] P. Del Gaudio, G. Auriemma, P. Russo, T. Mencherini, P. Campiglia, M. Stigliani, et al., Novel co-axial prilling technique for the development of core–shell particles as delayed drug delivery systems, Eur. J. Pharm. Biopharm. 87 (2014) 541–547, https://doi.org/10.1016/j.ejpb.2014.02.010.
[37] P. Apiwattanasiri, R. Charoen, S. Rittisak, K. Phattayakorn, S. Jantrasee, W. Savedboworn, Co-encapsulation efficiency of silk sericin-alginate-prebiotics and the effectiveness of silk sericin coating layer on the survival of probiotic Lactobacillus casei, Food Biosci. 46 (2022) 101576, https://doi.org/10.1016/j.fbio.2022.101576.
[38] H. Ge, J. Chen, Z. Ren, R. Zhu, R. Limanowski, Impact of viscosity ratio on the mixing efficiency of a core–shell structured droplet micromixer, Microfluid. Nanofluid. 26 (2022) 89, https://doi.org/10.1007/s10404-022-02595-3.
[39] R. Pereira, A. Tojeira, D.C. Vaz, A. Mendes, P. Bártolo, Preparation and characterization of films based on alginate and aloe vera, Int. J. Polym. Anal. Charact. 16 (2011) 449–464, https://doi.org/10.1080/1023666X.2011.599923.
[40] H. Lee, S.J. Park, M. Lee, K. Choi, H.Y. Choi, Y. Hasegawa, et al., Fabrication of nanofibers using fibroin regenerated by recycling waste silk selvage, Polym. Bull. 77 (2020) 3853–3862, https://doi.org/10.1007/s00289-020-03113-7.
[41] G. Ozesme Taylan, C. Illanes-Bordomás, O. Guven, E. Erkan, S.Ç. Erünsal, M. H. Oztop, et al., Core-shell aerogel design for enhanced oral insulin delivery, Int. J. Pharm. 669 (2025) 125038, https://doi.org/10.1016/j.ijpharm.2024.125038.
[42] S. Baptista-Silva, B.G. Bernardes, S. Borges, I. Rodrigues, R. Fernandes, S. Gomes-Guerreiro, et al., Exploring silk sericin for diabetic wounds: an in situ-forming hydrogel to protect against oxidative stress and improve tissue healing and regeneration, Biomolecules 12 (2022) 801, https://doi.org/10.3390/biom12060801.
[43] F. Abasalizadeh, S.V. Moghaddam, E. Alizadeh, E. akbari, E. Kashani, S.M. B. Fazljou, et al., Alginate-based hydrogels as drug delivery vehicles in cancer treatment and their applications in wound dressing and 3D bioprinting, J. Biol. Eng. 14 (2020) 8, https://doi.org/10.1186/s13036-020-0227-7.
[44] Y. Cao, F. Liu, Y. Chen, T. Yu, D. Lou, Y. Guo, et al., Drug release from core-shell PVA/silk fibroin nanoparticles fabricated by one-step electrospraying, Sci. Rep. 7 (2017) 11913, https://doi.org/10.1038/s41598-017-12351-1.
[45] P.J.M. Van Galen, H.W.T. Van Vlijmen, A.P. IJzerman, W. Soudijn, A model for the antagonist binding site on the adenosine A1 receptor, based on steric, electrostatic, and hydrophobic properties, J. Med. Chem. 33 (1990) 1708–1713, https://doi.org/10.1021/jm00168a027.
[46] S.-K. Kim, Z.-G. Gao, P. Van Rompaey, A.S. Gross, A. Chen, S. Van Calenbergh, et al., Modeling the adenosine receptors: comparison of the binding domains of A2A agonists and antagonists, J. Med. Chem. 46 (2003) 4847–4859, https://doi.org/10.1021/jm0300431.
[47] R. Gomes Daré, A. Beatriz Chieco Costa, T. Silva Martins, L.B. Lopes, Simvastatin and adenosine-co-loaded nanostructured lipid carriers for wound healing: development, characterization and cell-based investigation, Eur. J. Pharm. Biopharm. 205 (2024) 114533, https://doi.org/10.1016/j.ejpb.2024.114533.
[48] D.M. Silva, R. Liu, A.F. Gonçalves, A. da Costa, A. Castro Gomes, R. Machado, et al., Design of polymeric core-shell carriers for combination therapies, J. Colloid Interface Sci. 587 (2021) 499–509, https://doi.org/10.1016/j.jcis.2020.12.001.
[49] S. Nayak, S. Dey, S.C. Kundu, Silk sericin–alginate–chitosan microcapsules: hepatocytes encapsulation for enhanced cellular functions, Int. J. Biol. Macromol. 65 (2014) 258–266, https://doi.org/10.1016/j.ijbiomac.2014.01.042.
[50] X. Wu, Z. Tang, X. Liao, Z. Wang, H. Liu, Fabrication of chitosan@calcium alginate microspheres with porous core and compact shell, and application as a quick traumatic hemostat, Carbohydr. Polym. 247 (2020) 116669, https://doi.org/10.1016/j.carbpol.2020.116669.
[51] D. González-Restrepo, A. Zuluaga-Vélez, L.M. Orozco, J.C. Sepúlveda-Arias, Silk fibroin-based dressings with antibacterial and anti-inflammatory properties, Eur. J. Pharm. Sci. 195 (2024) 106710, https://doi.org/10.1016/j.ejps.2024.106710.
[52] G. Haskó, B. Cronstein, Regulation of inflammation by adenosine, Front. Immunol. 4 (2013) 85, https://doi.org/10.3389/fimmu.2013.00085.
[53] L. Chen, X. Lei, K. Mahnke, Adenosine and its receptors in the pathogenesis and treatment of inflammatory skin diseases, Int. J. Mol. Sci. 25 (2024) 5810, https://doi.org/10.3390/ijms25115810.
[54] M.C. Montesinos, A. Desai, J.-F. Chen, H. Yee, M.A. Schwarzschild, J.S. Fink, et al., Adenosine promotes wound healing and mediates angiogenesis in response to tissue injury via occupancy of A2A receptors, Am. J. Pathol. 160 (2002) 2009–2018, https://doi.org/10.1016/S0002-9440(10)61151-0.
[55] V.P. Ribeiro, J. Silva-Correia, A.I. Nascimento, A. da Silva Morais, A.P. Marques, A. S. Ribeiro, et al., Silk-based anisotropical 3D biotextiles for bone regeneration,

Biomaterials 123 (2017) 92–106, https://doi.org/10.1016/j.biomaterials.2017.01.027.
[56] D. Heimes, N. Wiesmann-Imilowski, T. Heidebrecht, S. Blatt, A. Pabst, P. Becker, et al., Biofunctionalization of silk fibroin scaffolds with enamel matrix protein and injectable platelet rich fibrin for soft tissue augmentation: an in-ovo study, Int. J. Implant Dent. 11 (2025) 13, https://doi.org/10.1186/s40729-025-00601-1.
[57] T. Watchararot, N. Soomherun, J. Jitpibull, S. Keeratihattayakorn, J. Ratanavaraporn, Antibacterial, angiogenic and irritation evaluation of mupirocin-loaded silk fibroin hydrogel, J. Drug Delivery Sci. Technol. 108 (2025) 106910, https://doi.org/10.1016/j.jddst.2025.106910.
[58] I. Feoktistov, A.E. Goldstein, S. Ryzhov, D. Zeng, L. Belardinelli, T. Voyno-Yasenetskaya, et al., Differential expression of adenosine receptors in human endothelial cells, Circ. Res. 90 (2002) 531–538, https://doi.org/10.1161/01.RES.0000012203.21416.14.
[59] K. Saravanakumar, A. Sathiyaseelan, X. Zhang, S. Park, M.-H. Wang, Purinoceptor targeted cytotoxicity of adenosine triphosphate-conjugated biogenic selenium nanoparticles in human colon cancer cells, Pharmaceuticals 15 (2022) 582, https://doi.org/10.3390/ph15050582.